
Article:
Kumar, M., Murawski, K., Kuźma, B. et al. (2024) Numerical experiment on the influence of granulation-induced waves on solar chromosphere heating and plasma outflows in a magnetic arcade. The Astrophysical Journal, 975 (1). 3. ISSN: 0004-637X

https://doi.org/10.3847/1538-4357/ad7464

The Astrophysical Journal, 975:3 (10pp), 2024 November 1 https://doi.org/10.3847/1538-4357/ad7464

Numerical Experiment on the Influence of Granulation-induced Waves on Solar Chromosphere Heating and Plasma Outflows in a Magnetic Arcade

M. Kumar[1,2], K. Murawski[1], B. Kuźma[3], E. K. J. Kilpua[2], S. Poedts[1,4], and R. Erdélyi[5,6,7]
[1] Institute of Physics, University of M. Curie-Skłodowska, Pl. M. Curie-Skłodowskiej 1, 20-031 Lublin, Poland
[2] Particle Physics and Universe Sciences (PAPU), Department of Physics, University of Helsinki, 00014, Helsinki, Finland
[3] Shenzhen Key Laboratory of Numerical Prediction for Space Storm, Institute of Space Science and Applied Technology, Harbin Institute of Technology, Shenzhen, 51805, People's Republic of China; kuzma@hit.edu.cn
[4] Department of Mathematics/Centre for Mathematical Plasma Astrophysics, KU Leuven, 3001 Leuven, Belgium
[5] Solar Physics and Space Plasma Research Centre (SP^{2}RC), School of Mathematics and Statistics, University of Sheffield, Hounsfield Road, Hicks Building, Sheffield, S3 7RH, UK
[6] Department of Astronomy, Eötvös Loránd University, Pázmány Péter sétány 1/A, H-1112 Budapest, Hungary
[7] Hungarian Solar Physics Foundation, Petőfi tér 3, H-5700 Gyula, Hungary
Received 2024 April 12; revised 2024 July 21; accepted 2024 August 26; published 2024 October 21

Abstract

This paper offers a fresh perspective on solar chromosphere heating and plasma outflows, focusing on the contribution of waves generated by solar granulation. Utilizing a 2.5D numerical experiment for the partially ionized lower solar atmosphere, we investigate the dissipation of these waves and their impact on plasma outflows and chromospheric heating via ion-neutral collisions. Employing the JOint ANalytical and Numerical Approach code, we adopt two-fluid model equations, examining partially ionized hydrogen plasma dynamics, including protons+electrons and neutrals, treated as two separate fluids that are coupled through ion-neutral collisions. Our investigation focuses on a quiet solar chromosphere region characterized by gravitational stratification and magnetic confinement by an initially set single magnetic arcade. The primary source of the waves is the solar convection beneath the photosphere. Our results demonstrate that ion-neutral collisions result in the dissipation of such waves, releasing thermal energy that heats the chromosphere plasma. Notably, this is accompanied by upward-directed plasma flows. Finally, we conclude that wave dissipation due to ion-neutral collisions in the two-fluid plasma model induces chromosphere heating and plasma outflows.

Unified Astronomy Thesaurus concepts: Solar physics (1476); The Sun (1693); Solar chromosphere (1479); Solar photosphere (1518); Solar wind (1534); Magnetohydrodynamics (1964)

1. Introduction

The origin of the thermal energy that drives the heating of the different layers of the solar atmosphere has long been at the center of solar physics research. Across the decades, several potential mechanisms have been established as sources of heating of the solar atmosphere. One conceivable energy transport scenario involves the plasma motions in the convective layer and the global oscillations of the Sun's surface that could trigger magnetohydrodynamic (MHD) waves that subsequently transport energy from the photosphere into the higher solar atmosphere. These waves could propagate through the chromosphere into the corona, effectively transporting energy that could be thermalized higher up by their dissipation. Many studies considering waves in a two-fluid plasma have been performed in the past (e.g., D. B. Jess et al. 2009; S. Yang & Y. Xiang 2016; Y. G. Maneva et al. 2017; N. Yadav et al. 2021). In the solar atmosphere, ion-neutral collisions can dampen the waves (R. Soler et al. 2015; P. G. Judge 2020), thus converting part of the wave energy into thermal energy, which may sustain the temperature of the solar chromosphere. J. H. Piddington (1956) and D. E. Osterbrock (1961) performed earlier studies on solar atmosphere heating by ion-neutral collisions. J. E. Leake et al. (2005) investigated the propagation of Alfvén waves (H. Alfvén 1942) within the MHD framework. R. Soler et al. (2014) studied Alfvén waves by considering ion-neutral collisions. The authors investigated wave damping as a function of height. They compared the results of two sets of collision cross sections, namely hard-sphere cross sections and quantum mechanical cross sections. Along similar lines, M. Khodachenko et al. (2004) performed a comparative study of the MHD wave damping in the solar atmosphere due to the collisional dissipation (mainly associated with resistivity) and viscous dissipation mechanisms. Their study concludes that collisional dissipation is more effective than viscous effects, and thermal conductivity affects the damping of MHD waves. S. I. Braginskii (1965) provided a detailed discussion of the transport processes in a plasma.

Recently, some parametric studies have also been performed. For instance, M. Pelekhata et al. (2021) concluded from a parametric study that the dissipation of large-amplitude Alfvén waves due to ion-neutral collisions contributes to chromosphere heating. Some authors have also explored the nonlinear transformation of waves into shocks. For example, R. Niedziela et al. (2021) suggested that magnetoacoustic waves (MAW) may transform into shocks and heat the chromosphere, considering ion-neutral collisions. M. Kumar et al. (2023) extended the model of M. Pelekhata et al. (2021) and R. Niedziela et al. (2021) by taking coupled Alfvén and MAWs into account. The authors concluded that coupled Alfvén MAWs are more effective in heating the solar chromosphere than MAWs alone. Similar studies by B. Kuźma et al. (2019) inferred that the heating by Alfvén waves is inadequate to compensate for the chromosphere radiative losses. These

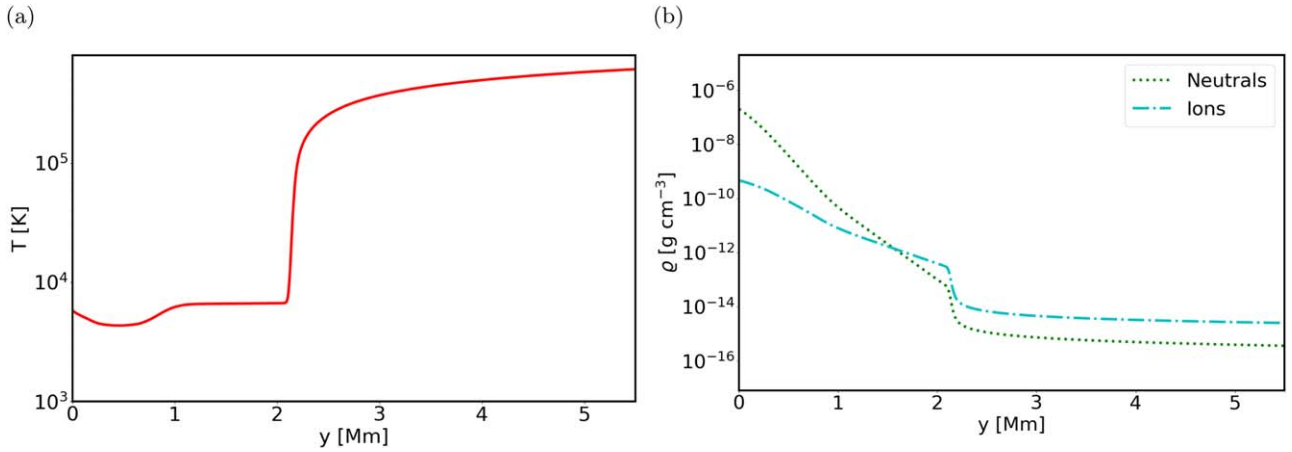

Figure 1. Vertical profiles of (a) equilibrium temperature (T), taken from the model of E. H. Avrett & R. Loeser (2008), initially set equal for ions and neutrals (thermal equilibrium); and (b) the mass density of ions (dots) and neutrals (dashes) for the initial magnetohydrostatic equilibrium configuration. At the beginning (i.e., at $t = 0$ s), the ion (T_i) and neutral (T_n) temperatures are the same, but later, this condition is relaxed and T_i, T_n are allowed to undergo variation.

authors suggest that waves originating from the solar convection zone develop into shocks that efficiently release their energy into the background medium. Besides, the work by Y. Wang et al. (2021) delved into the dissipation of fast magnetoacoustic shock waves in the low-β chromosphere. The findings of these authors revealed a balance between the heating rate and radiative losses, emphasizing the substantial role these shock waves play in energizing and heating the chromosphere.

A topic that has recently received plenty of attention is the triggering of waves by solar granulation and the potential role of these waves in energy transport and heating. Granulation is a complex phenomenon occurring in the quiet regions of the solar atmosphere that starts below the photosphere and extends above the chromosphere (R. Stein & Å. Nordlund 1998). In the photosphere, granules are observed as bright cells with darker boundaries caused by convective motions of plasma. However, as these granules extend above the solar minimum region into higher atmospheric layers, their appearance changes; they become less visible and exhibit a reversed brightness pattern, with dark cores and bright lanes. This dynamic process is a significant source of compressible waves that traverse the higher layers of the solar atmosphere (R. F. Stein & J. Leibacher 1974). These waves, initially driven by convective motions under the photosphere, can interact and superpose to form larger-scale global modes. The combination of these global modes has the potential to produce shocks, which are distinctly seen in the chromosphere (B. Lites et al. 1993; P. G. Judge et al. 2001). T. J. Bogdan et al. (2003) highlighted the complexity behind identifying the source of such waves in the solar convection zone, due to its intricate dynamics. D. Wójcik et al. (2020) investigated waves in the two-fluid plasma resulting from spontaneously evolving and self-organizing convection-forming granulation cells. Their findings indicated that these waves efficiently heat the plasma, thereby being capable of compensating for radiative and thermal energy losses. These authors also reported for the very first time an agreement with an observationally based semi-empirical model without the need to involve heating by shock waves. In addition, K. Murawski et al. (2022) performed a comparative study of 2D and 3D numerical simulations of two-fluid jets and waves excited by the granulation in a partially ionized solar atmosphere. The findings of these authors also align with observational data, and they concluded that the heating resulting from ion-neutral collisions compensates for the radiative energy losses. However, M. Carlsson & R. F. Stein (1994) suggest that the initial assumptions of the semi-empirical model may not fully capture the dynamic behavior of the solar atmosphere under time-dependent conditions.

Two-fluid granulation-generated waves were also investigated in a solar magnetic arcade by B. Kuźma et al. (2021a) in the context of the spatial variation of wave periods in a solar magnetic arcade. Here, the authors focused on the impact of two-fluid effects on the periods of the propagating ion magnetoacoustic-gravity and neutral acoustic-gravity waves. Similarly, K. Murawski et al. (2022) provided a comprehensive understanding of how granulation in the two-fluid plasma generates wave propagation and plasma flows. This process leads to the heating driven by the dissipation of neutral acoustic-gravity waves, Alfvén waves, and magnetoacoustic-gravity waves in the nonideal quiet solar atmosphere. These effects arise mainly due to nonideal processes such as ion-neutral collisions.

Motivated by the abovementioned studies and open questions, in the present article, we focus on the quiet regions of the photosphere. The primary objective of this study is to extend the model of K. Murawski et al. (2022) in the framework of a symmetric, stratified, and isolated magnetic arcade, while excluding the consideration of ionization/recombination. We will focus on solar granulation and investigate how collisions between different plasma species dampen the granulation-excited waves and the subsequent role these waves can play in heating the upper solar chromosphere. Our numerical results aim to look into the fundamental process affecting the waves in the two-fluid plasma approximation in the described magnetic arcade, along with their contribution to the plasma outflows.

The structure of this paper is outlined as follows. Section 2 describes the set of governing equations. Section 3 includes the numerical setup. Section 4 presents the corresponding numerical results and, last, Section 5 encapsulates both a summary and discussion of the results presented in this paper.

2. Two-fluid Numerical Model and Governing Equations

Due to the relatively low temperatures (Figure 1(a)), the photosphere and chromosphere are only partially ionized. Consequently, a two-fluid model is more suitable for studying

wave-driven processes in the partially ionized solar atmosphere. Therefore, in the considered two-fluid plasma model, we focus on the quiet region of the solar atmosphere, extended from the top of the convective zone to the low solar corona, characterizing it as partially ionized (e.g., T. V. Zaqarashvili et al. 2011; E. Khomenko et al. 2014), gravitationally stratified, and magnetically confined. The significance of studying the waves in the quiet regions of the Sun is to gain insights into the overall behavior of how waves propagate, dissipate, and transfer energy in these regions, which are more prevalent than in the active regions. The ongoing processes during wave propagation and dissipation may have implications for the heating and dynamics of the solar atmosphere. We assume that the initial physical quantities (e.g., temperature and mass density—Figures 1(a) and (b)) vary according to the model of E. H. Avrett & R. Loeser (2008). Specifically, we consider a two-component composition of the solar atmosphere: protons +electrons and neutrals (H atoms) coupled by ion-neutral collisions (J. L. Ballester et al. 2018). In the following equations (Equations (1)–(12)), the corresponding counterparts for ions and neutrals are denoted by the subscripts "i" and "n," respectively. In the current model version, it is important to note that, unlike the model by K. Murawski et al. (2022), the self-consistent evolution of ionization and recombination processes is not incorporated. Instead, only the total numbers of ions+electrons and neutrals are considered. The exclusion of ionization/recombination in this study reduces the complexity of the model. It allows us to study the role of ion-neutral collisions in a better controlled numerical experiment, ultimately further emphasizing their role in the partially ionized solar atmosphere. These distinct fluid components adhere to a set of governing equations (T. V. Zaqarashvili et al. 2011; J. E. Leake et al. 2014; Y. G. Maneva et al. 2017; K. Murawski et al. 2022 and references therein):

(a) the equations of mass conservation:

$$\frac{\partial \varrho_{\rm i}}{\partial t} + \nabla \cdot (\varrho_{\rm i} \boldsymbol{V}_{\rm i}) = 0, \tag{1}$$

$$\frac{\partial \varrho_{\rm n}}{\partial t} + \nabla \cdot (\varrho_{\rm n} \boldsymbol{V}_{\rm n}) = 0; \tag{2}$$

(b) the equations of momentum conservation:

$$\frac{\partial (\varrho_{\rm i} \boldsymbol{V}_{\rm i})}{\partial t} + \nabla \cdot (\varrho_{\rm i} \boldsymbol{V}_{\rm i} \boldsymbol{V}_{\rm i} + p_{\rm ie} \boldsymbol{I}) - \frac{1}{\mu} (\nabla \times \boldsymbol{B}) \times \boldsymbol{B} = \varrho_i \boldsymbol{g} + \nabla \cdot \boldsymbol{\Pi}_{\rm i} + \boldsymbol{S}_{\rm i}, \tag{3}$$

$$\frac{\partial (\varrho_{\rm n} \boldsymbol{V}_{\rm n})}{\partial t} + \nabla \cdot (\varrho_{\rm n} \boldsymbol{V}_{\rm n} \boldsymbol{V}_{\rm n} + p_{\rm n} \boldsymbol{I}) = \varrho_{\rm n} \boldsymbol{g} + \nabla \cdot \boldsymbol{\Pi}_{\rm n} + \boldsymbol{S}_{\rm n}; \tag{4}$$

and (c) the equations of energy conservation:

$$\frac{\partial E_{\rm i}}{\partial t} + \nabla \cdot \left[\left(E_{\rm i} + p_{\rm ie} + \frac{\boldsymbol{B}^2}{2\mu} \right) \boldsymbol{V}_{\rm i} - \frac{\boldsymbol{B}}{\mu} (\boldsymbol{V}_{\rm i} \cdot \boldsymbol{B}) \right] + \nabla \cdot \left[\frac{\eta}{\mu} (\nabla \times \boldsymbol{B}) \times \boldsymbol{B} \right] = (\varrho_{\rm i} \boldsymbol{g} + \boldsymbol{S}_{\rm i}) \cdot \boldsymbol{V}_{\rm i} + Q_{\rm i} + \nabla \cdot (\boldsymbol{V}_{\rm i} \cdot \Pi_{\rm i}) + q_{\rm i} - L_{\rm r}, \tag{5}$$

$$\frac{\partial E_{\rm n}}{\partial t} + \nabla \cdot [(E_{\rm n} + p_{\rm n}) \boldsymbol{V}_{\rm n})] = (\varrho_{\rm n} \boldsymbol{g} + \boldsymbol{S}_{\rm n}) \cdot \boldsymbol{V}_{\rm n} + Q_{\rm n} + \nabla \cdot (\boldsymbol{V}_{\rm n} \cdot \Pi_{\rm n}) + q_{\rm n} - L_{\rm n}. \tag{6}$$

Here, the energy densities ($E_{\rm i,n}$) are given by

$$E_{\rm i} = \frac{\varrho_{\rm i} \boldsymbol{V}_{\rm i}^2}{2} + \frac{p_{\rm ie}}{\gamma - 1} + \frac{\boldsymbol{B}^2}{2\mu}, \tag{7}$$

$$E_{\rm n} = \frac{\varrho_{\rm n} \boldsymbol{V}_{\rm n}^2}{2} + \frac{p_{\rm n}}{\gamma - 1}. \tag{8}$$

The momentum collisional terms, $\boldsymbol{S}_{\rm i,n}$, are specified as

$$\boldsymbol{S}_{\rm i} = \alpha_{\rm in} (\boldsymbol{V}_{\rm n} - \boldsymbol{V}_{\rm i}), \tag{9}$$

$$\boldsymbol{S}_{\rm n} = \alpha_{\rm in} (\boldsymbol{V}_{\rm i} - \boldsymbol{V}_{\rm n}). \tag{10}$$

The heat production/exchange terms for the ion and neutral collisions, $Q_{\rm i,n}$, are specified as

$$Q_{\rm i} = \frac{\alpha_{\rm in}}{2} (\boldsymbol{V}_{\rm n} - \boldsymbol{V}_{\rm i})^2 + \frac{1}{\gamma - 1} \frac{k_{\rm B} \alpha_{\rm in}}{m_{\rm i} + m_{\rm n}} (T_{\rm n} - T_{\rm i}) \tag{11}$$

and

$$Q_{\rm n} = \frac{\alpha_{\rm in}}{2} (\boldsymbol{V}_{\rm n} - \boldsymbol{V}_{\rm i})^2 + \frac{1}{\gamma - 1} \frac{k_{\rm B} \alpha_{\rm in}}{m_{\rm n} + m_{\rm i}} (T_{\rm i} - T_{\rm n}). \tag{12}$$

The first terms of Equations (11) and (12) denote collisional plasma heating (J. L. Ballester et al. 2018). In the present model, these terms remain important in the context of plasma heating, which results from inelastic collisions between ions and neutrals. Such collisions contribute to plasma heating through friction-like dissipation due to the relative motion between ions and neutrals, converting wave energy into thermal energy and effectively heating the plasma. Other terms are connected with the thermal energy exchange between ions and neutrals. The above equations are supplemented by the induction equation and Ohm's law (see, e.g., Y. G. Maneva et al. 2017), which are respectively given as

$$\frac{\partial \boldsymbol{B}}{\partial t} = -\nabla \times \boldsymbol{E}, \tag{13}$$

$$\boldsymbol{E} + \boldsymbol{V}_{\rm i} \times \boldsymbol{B} = \eta \boldsymbol{j}, \tag{14}$$

with $\boldsymbol{E}, \boldsymbol{j}$ being the electric field and current density, with the solenoidal constraint $\nabla \cdot \boldsymbol{B} = 0$. Since the mass of electrons is much smaller than the mass of ions and neutrals, we omit all terms associated with electron inertia in Ohm's law (J. L. Ballester et al. 2018).

In Equations (1)–(12), each fluid component is characterized by its number density ($n_{\rm i,n}$), mass density $\varrho_{\rm i,n} = n_{\rm i,n} m_{\rm i,n}$ (here, $m_{\rm i} = m_{\rm n} = m_{\rm H}$ are the masses of ions and neutrals, with $m_{\rm H}$ being the hydrogen atom mass), temperature ($T_{\rm i,n}$), velocity ($\boldsymbol{V}_{\rm i,n}$), and gas pressure ($p_{\rm ie,n}$), with $p_{\rm ie} = p_{\rm i} + p_{\rm e} = 2p_{\rm i}$. For an ideal monoatomic gas, the adiabatic index (γ) is taken as equal to 5/3, and the acceleration due to gravity on the surface of the Sun ($\boldsymbol{g}$), with a magnitude of 274.78 m s^{-2}, points in the negative y-direction. The magnetic induction and the magnetic permeability of the medium are denoted, respectively, by $\boldsymbol{B}$ and μ. The coefficient of magnetic resistivity and the viscosity tensor are, respectively, symbolized by η and $\boldsymbol{\Pi}_{\rm i,n}$ (J. E. Leake et al. 2012). The radiative loss term ($L_{\rm r}$) is implemented here, approximated as the thick radiation justified in the lower layers of the solar atmosphere (W. P. Abbett & G. H. Fisher 2012). In contrast, thin radiation operates in the upper solar layers (R. Moore & P. Fung 1972). The thermal conductivity terms are denoted by $q_{\rm i,n}$ (L. Spitzer 1962). The ion-neutral collision coefficient ($\alpha_{\rm in}$) is given as (J. L. Ballester et al.

2018; S. I. Braginskii 1965)

$$\alpha_{\rm in} = \frac{4}{3}\frac{\sigma_{\rm in}\varrho_{\rm i}\varrho_{\rm n}}{(m_{\rm i}+m_{\rm n})}\sqrt{\frac{8k_{\rm B}}{\pi}\left(\frac{T_{\rm i}}{m_{\rm i}}+\frac{T_{\rm n}}{m_{\rm n}}\right)}. \quad (15)$$

Here, $\sigma_{\rm in} = 1.4\times10^{-19}\,{\rm m}^2$ represents the ion-neutral quantum collisional cross section (J. Vranjes & P. S. Krstic 2013). We note that the current model does not consider charge transfer collisions, which have not yet been implemented in the JOint ANalytical and Numerical Approach (JOANNA) code. Collisions involving momentum-changing charge transfer do not result in energy changes. This matters because one must carefully include irreversible processes in the heating rates $Q_{\rm i,n}$ (Equations (11) and (12)). The relation between $\varrho_{\rm i,n}$, $T_{\rm i,n}$, and $p_{\rm i,n}$ is given by the ideal gas laws as follows:

$$p_{\rm i,n} = \frac{k_{\rm B}}{m_{\rm i,n}}\varrho_{\rm i,n}T_{\rm i,n}, \quad (16)$$

where $k_{\rm B}$ is the Boltzmann constant and the other symbols have their usual meanings. In the context of the presented two-fluid model, our analysis focuses on examining key physical attributes related to the dynamics of ions. This includes investigating parameters like the ion velocity (vertical component), the temperature of ions, and the period of the waves excited in two-fluid plasma, as described in Section 4.

2.1. Magnetohydrostatic Equilibrium in the Solar Atmosphere Model

Before conducting a series of numerical experiments, all physical quantities such as gas pressure, temperature, mass density, velocity, etc. are assumed to be in magnetohydrostatic equilibrium and, hence, invariant in time (i.e., $\partial f/\partial t = 0$, where f stands for any equilibrium plasma quantity). Since the initially considered magnetic field is current-free ($\nabla\times\boldsymbol{B}/\mu = 0$) and thus (Lorentz)-force-free ($(\nabla\times\boldsymbol{B}/\mu)\times\boldsymbol{B} = 0$), the condition of hydrostatic magnetic equilibrium prevails when the gradient of the outward force caused by the gas pressure equalizes the gravitational inward pull. This magnetohydrostatic equilibrium can be derived from Equations (3)–(4), by setting both $\boldsymbol{V}_{\rm i,n}$ and the Lorentz force equal to zero (D. Wójcik et al. 2019a). The obtained mathematical expression is

$$\nabla p_{\rm i,n} = \varrho_{\rm i,n}\,\mathbf{g}. \quad (17)$$

Panel (a) of Figure 1 shows the initial equilibrium temperature versus height above the solar surface (notice the logarithmic vertical scale). Panel (b) illustrates the mass density profiles for ions (dotted green line) and neutrals (dashed–dotted blue line) as a function of height from the quiet solar atmosphere model of E. H. Avrett & R. Loeser (2008), who investigated the degree to which their model could explain the quiet-Sun EUV line and continuum spectra. Initially (i.e., at $t = 0$ s), the temperatures of the ions ($T_{\rm i}$) and neutrals ($T_{\rm n}$) are assumed to be equal, i.e., there is an initial thermal balance between ions and neutrals; but later on, this assumption is relaxed, so that ions and neutrals are allowed to have different temperatures. This assumption is motivated by the fact that the plasma is well mixed due to frequent collisions between various species, which in turn induces temperature equilibrium. In other words, assuming a single temperature is a suitable estimate for the average behavior of the plasma and aids in simplifying the present model (e.g., see, Y. G. Maneva et al. 2017; D. Wójcik et al. 2018). However, as far as numerical experiments on solar granulation are concerned, the initial hydrodynamic state does not play that much role in the system's evolution. A more adequate chosen initial state might shorten the relaxation time required for the system to transition into the developed turbulence; conversely, a more convectively stable initial state could lengthen this period, as the system would take longer to reach the quasi-stationary state with the granulation and all other phenomena associated with it. What influences the system's evolution that matters more is the topology of the magnetic field and its strength. Moreover, in our early two-fluid models, assumptions such as $T_{\rm i}\neq T_{\rm n}$ were also considered, such as by B. Kuźma et al. (2017).

The approximate temperature minimum of 4300 K occurs in the lower layers of the chromosphere (i.e., $y\approx0.6$ Mm; Figure 1(a)). Note that as a result of the lower temperature, a considerable amount of neutrals are present in this region, which is clearly visible in Figure 1(b), where the green dotted line lies considerably above the blue dashed–dotted line. Therefore, the contributions of the neutrals are also taken into account to realistically represent the chromospheric medium in the present model (T. V. Zaqarashvili et al. 2011). Additionally, the presence of such neutral atoms in the partially ionized plasma of the lower solar photosphere and chromosphere further enhances the efficiency of the energy dissipation mechanism of excited waves.

The sharp rise in temperature occurs at the relatively narrow transition region ($y\approx2.1$ Mm) between the chromosphere and the corona. Above $y\approx4$ Mm, the temperature growth slows down considerably, and the temperature profile almost flattens. Due to this sudden rise in temperature at the transition region (i.e., $y\approx2.1$ Mm), the ionization degree increases, and the mass density of ions overtakes that of neutrals at $y\approx2.1$ Mm, as visible in Figure 1(b). Initially (i.e., at $t = 0$ s), we set all plasma quantities to their equilibrium values at the top and bottom boundaries (i.e., in the y-direction), while at the lateral sides (i.e., in the $x-$direction), we impose periodic boundary conditions. The magnetohydrostatic profiles give the initial conditions for $\varrho_{\rm i,n}$ and $\rm P_{i,n}$ (Equation (14)), which are overlaid by the following potential magnetic structure with closed magnetic lines which that initially (i.e., at $t = 0$) resembles an arcade (B. Low 1985). This curved structure of magnetic field lines connects two regions of opposite polarity on the quiet region of the solar surface (Figure 2(a)):

$$B_x = B_{\rm a}\cos\left(\frac{x}{\Lambda_{\rm B}}\right)\exp\left(-\frac{y}{\Lambda_{\rm B}}\right), \quad (18)$$

$$B_y = -B_{\rm a}\sin\left(\frac{x}{\Lambda_{\rm B}}\right)\exp\left(-\frac{y}{\Lambda_{\rm B}}\right), \quad (19)$$

$$B_z = B_{\rm t}. \quad (20)$$

Here, $B_{\rm a} = 4$ G is the spatially averaged magnetic field strength of the arcade structure at the solar surface (i.e., $y = 0$ Mm). It is also important to emphasize that magnetic field strengths in the photosphere can reach much higher values (1000–2000 G), mainly due to compression in the granule lanes. However, the field value adopted in the present mode represents the magnetic flux per unit area (Mx cm^{-2}) that corresponds to the expanded magnetic field observed in the quieter region of the solar atmosphere. While our model does not capture the highly localized and intense magnetic fields at granular scales in the lower layers of the solar atmosphere, it does however describe

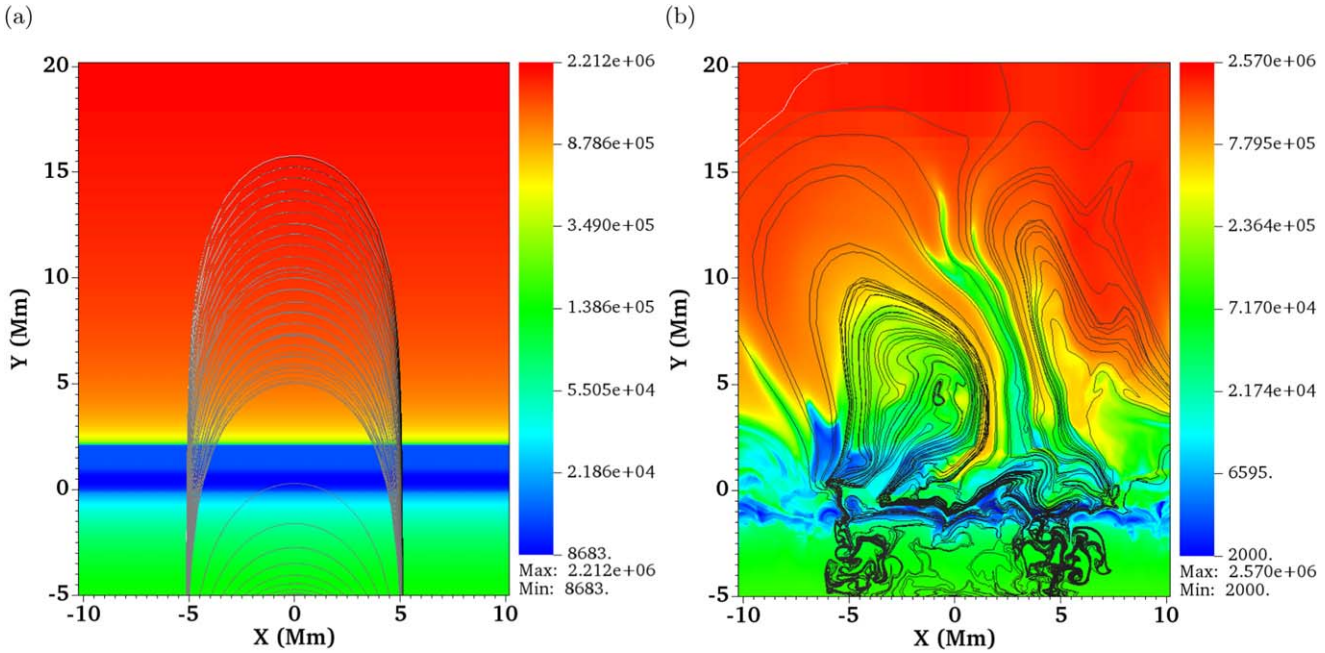

Figure 2. Spatial profiles of $\log T_i$ at two distinct time instances: (a) the initial state at $t = 0$ s and (b) the evolved state at $t = 8870$ s. In panel (a), the spatial profile illustrates the characteristics of an unperturbed magnetic arcade, as described by Equations (18)–(20). In contrast, panel (b) shows the spatial profile of an evolved magnetic arcade. The figures demonstrate the temperatures of the ions across the spatial domain at two instances of time.

the more diffused magnetic fields in higher layers, consistent with the physical phenomena observed in the quiet Sun (S. Shelyag et al. 2012; E. Priest 2014). Therefore, the above values are consistent with the physical phenomena observed in the solar atmosphere. The symbol $B_t = 2$ G denotes the transversal component of the magnetic field (Z. Yang et al. 2020), $\Lambda_B = 2L/\pi$ is the magnetic scale height, and $L = 5.12$ Mm is the half-width of the arcade. Note that the photosphere is initially permeated by a single magnetic arcade, with its footpoints fixed at $x = -5.12$ Mm and $x = 5.12$ Mm, well rooted in the dense convective zone and expanding into the photosphere, chromosphere, and lower corona.

3. Numerical Setup

Numerical experiments are performed to investigate the propagation of granulation-generated waves, their dissipation, and the corresponding heating in the gravitationally stratified and partially ionized solar atmosphere (J. L. Ballester et al. 2018). We used the JOANNA code to solve the two-fluid equations in 2.5D Cartesian geometry described in Section 2, which is based upon the second-order Godunov-type method with the Harten–Lax–Van Leer discontinuities Riemann solver (T. Miyoshi & K. Kusano 2007; A. Mignone et al. 2009). This code uses the third-order super-stability-preserving Runge–Kutta method for temporal integration (D. R. Durran 2010). Note that this code has shown good agreement with observational data in recent works—for instance, as reported by D. Wójcik et al. (2020) and B. Kuźma et al. (2019). The condition of the magnetic monopole (Equation (11)) is maintained by the magnetic field cleaning method of A. Dedner et al. (2002). In the present study, we follow the Cartesian coordinate system, where $[x, y, z]$ stand, respectively, for the horizontal, vertical, and transversal components, unless otherwise stated. The 2D region of the computational box is described as $-10.24\,\mathrm{Mm} \leqslant x \leqslant 10.24$ Mm and $-3\,\mathrm{Mm} \leqslant y \leqslant 20$ Mm. Along the x-direction, the grid is divided uniformly into 1024 numerical cells, so that the size of each cell is $\Delta x = 20$ km.

In the vertical direction, the grid between -3 Mm $y \leqslant 7.24$ Mm is divided uniformly into 512 cells, resulting in a cell size of $\Delta y = 20$ km, while the region $5.12\,\mathrm{Mm} \leqslant y \leqslant 20$ Mm is elongated, by dividing it further into the 32 cells stretched in the y-direction (vertical). Note that the grid stretching for $y \geqslant 5.12$ Mm makes it behave like an absorbent, minimizing polluting reflections from the top border and simultaneously absorbing the incoming signal, which otherwise could interfere with the physical signal of interest. This numerical setup allows us to include a convectively unstable region just below the photosphere in the simulation. Therefore, the region of interest has a spatial resolution of $20\,\mathrm{km} \times 20\,\mathrm{km}$. In the numerical results that are being presented, we have shown the region of interest. In the whole experiment, the Courant–Friedrichs–Levy number is fixed at 0.9 (R. Courant et al. 1928).

The initial position (at $t = 0$ s) of the different layers of the solar atmosphere in the current model is as follows. The bottom and top of the photosphere are located at $y = 0$ Mm and $y = 0.5$ Mm, respectively. Similarly, the bottom and top of the chromosphere are at $y = 0.5$ Mm and $y = 2$ Mm, respectively. The transition region is situated in 2 Mm $\leqslant y \leqslant 2.1$ Mm. The total time duration for which we run our numerical simulation is 10^4 s.

4. Numerical Results

4.1. Chromospheric Heating

Over time, the solar granulation process dynamically alters the initial magnetohydrostatic equilibrium (Figures 1(a) and (b)). This distinctive pattern arises from the convectively unstable zone below the solar surface, as described in the introduction. The spatial profile depicting the logarithm of the

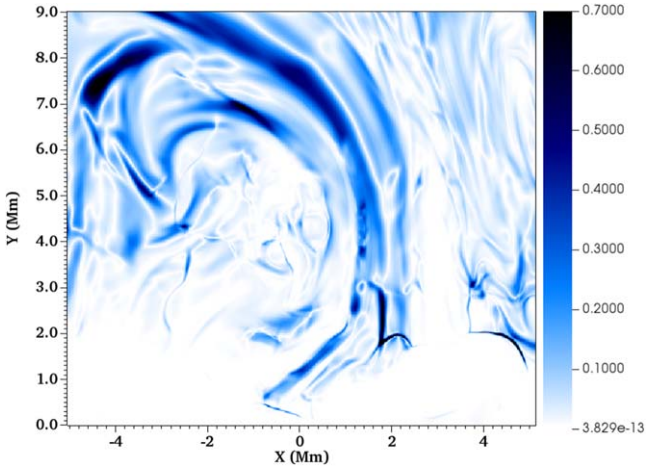

Figure 3. A snapshot depicting the spatial profile of $V_i - V_n$, measured in km s^{-1} at $t = 8870$ s. This visualization demonstrates the velocity drift across the spatial domain. The profile highlights our model's close connection between energy transport and the relative motion between ions and neutrals (see Equations (11)–(12)).

temperature of the ions (log T_i) expressed in K is showcased in Figure 2 (color map), capturing the states at $t = 0$ s (a) and $t = 8870$ s (b). We chose the latter time because it demonstrates the granulation and magnetic loops in their fully developed state. The spatial profile of log T_i here provides insight into both the hot and cool plasma and their corresponding temperature distribution across the spatial domain. Initially, the magnetic arcade rooted at $x = \pm 5.12$ Mm (as described by Equations (18)–(20)) remains essentially unperturbed (Figure 2(a)). Later on, the excited waves, such as the magnetoacoustic-gravity waves and the neutral acoustic-gravity waves (K. Murawski et al. 2013; B. Kuźma et al. 2021b), along with the motion of the photosphere plasma flows, induce a strong reconfiguration of the magnetic arcade in the solar atmosphere (small flux tubes; reshuffled black lines). The distorted magnetic field arcade is filled with hot and tenuous plasma. At a few locations, some magnetic fields can also be seen forming an extended vertical magnetic funnel (at $x \approx 5$ Mm), promoting the rise of plasma outflows. Such flux tubes act as guidelines for plasma outflows. Such upflows are also evident from the one-to-one correspondence with V_{iy} (Figure 5). Some cool plasma also descends back to the chromosphere, due to the gravitational force (Figure 5; blue patches). The two-fluid waves accompany both these upflows and downflows with dense and rarefied plasma, respectively. These waves travel upward and eventually enter the solar corona. Besides this, a few emerging jets are visible. The tallest jet extends to about $y \approx 15$ Mm. To its right, there is a thinner jet, while on the left side of the box, there is a smaller jet that leans to the left. A recent review by S. Skirvin et al. (2023) provides a detailed examination of jets and their formation in the solar lower atmosphere. S. James & R. Erdélyi (2002), S. James et al. (2003), and R. Erdélyi & S. P. James (2004) have conducted a series of studies on small-scale solar jets.

The present model considers ion-neutral collisions as the primary interaction, which mainly affects the motion of the ions and contributes to the overall heating of the solar atmosphere. In the arcade, where the magnetic field curvature is relatively high and the collision frequency is low, ion-neutral drift (i.e., $V_i - V_n$) reaches relatively higher values (Figure 3). The corresponding heating of the plasma, as a result of the ion-neutral collisions, can be inferred from the first term of the right-hand side of Equation (11). This term clearly implies it likely contributes to the observed heating in the upper layers of the solar atmosphere. A detailed study on the role of the dissipation of wave energy into thermal energy was performed by J. Martínez-Sykora et al. (2020). We note that the obtained characteristic features are a direct consequence of the natural convection processes taking place below the photosphere. Furthermore, due to the realignment of the magnetic field's footpoints, driven by granulation-induced convection, the ensuing plasma motions initiate magnetic reconfiguration that is well apparent, notably below the photosphere ($y \leqslant 0$; Figures 2(b) and 5).

In our model, the system undergoes an initial transient phase, lasting approximately 3000 s, followed by the attainment of a quasi-stationary state, before reaching $\max(t) = 10^4$ s. This quasi-equilibrium state periodically pushes the transition region upward and pulls downward from its initial position at $y \approx 2.1$, due to which oscillatory behavior emerges near the transition region. This behavior is evident in the time–distance plot of ion temperature presented in Figure 4(a), collected along the y-direction at $x = 0$. The time period for which the plot is shown corresponds to highlighting its quasi-equilibrium state, characterized by fully developed convection, occurring after the transient phase (not shown). We note that such a state emerges as a delicate balance between radiative cooling and the heating effects resulting from ion-neutral collisions.

Due to the presence of ion-neutral collisions, a fraction of the kinetic energy flux carried by excited waves gets thermalized in the solar atmosphere. Such thermalizations lead to localized variations in the temperature of the ions at different heights. Figure 4(b) illustrates the temporary average profile for the relative perturbation of the ion temperature $\delta T_i(y, t)/T(y) = (T_i(y, t) - T(y))/T(y)$, which is defined as

$$\left\langle \frac{\delta T_i(y, t)}{T(y)} \right\rangle_t = \frac{1}{t_2 - t_1} \int_{t_1}^{t_2} \frac{\delta T_i(y, t)}{T(y)}\, dt, \tag{21}$$

where $t_1 = 3500$ s and $t_2 = 9500$ s. Here, $T(y)$ is adapted from the semi-empirical model of E. H. Avrett & R. Loeser (2008), as shown in Figure 1(a). The plot signifies the deviation of the ion temperature from $T(y)$. This deviation provides insight into the dynamic nature of temperature perturbations (heating and cooling) in the solar chromosphere, resulting from the interaction of excited waves with plasma flows. The plot shows localized peaks in ion temperature perturbations at several locations. Notably, at $y \approx 1.5$ Mm, the sharp peak of $\delta T_i(y, t)/T(y) \approx 1.85$ indicates a significant localized heating event followed by a drop. This drop represents a rapid cooling or the spatial spreading of the localized heating event. From the plot, we observe an overall positive temperature perturbation, which clearly provides evidence of localized heating in the upper photosphere and chromosphere.

4.2. Plasma Outflows

The ongoing granulation process propels the cooler plasma beneath the photosphere toward the transition region and low solar corona, which may give rise to plasma outflows. The spatial profile of the vertical component of ion velocity (i.e., V_{iy}) is illustrated in Figure 5. This profile for V_{iy} provides a visualization of the dynamic nature of plasma in the various

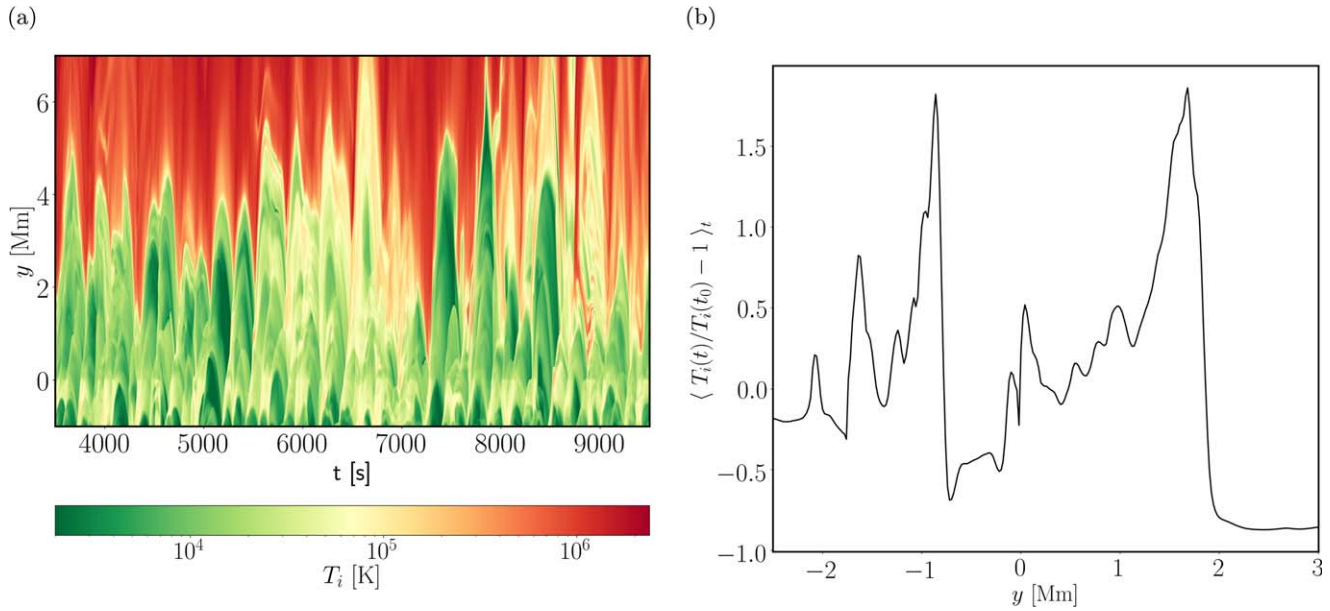

Figure 4. (a) Time–distance plots for the temperature of the ions (T_i), measured in Kelvins. This plot is evaluated from the slit taken along the y-direction, collected at $x = 0$ Mm, corresponding to Figure 2(b). The time-averaged profile of the relative ion temperature perturbation, $<\delta T_i(x = 0,\ y,\ t)/T(y)>_t$, is calculated as the deviation of $T_i(x = 0,\ y,\ t)$ from the model temperature $T(y)$, adopted from E. H. Avrett & R. Loeser (2008; Figure 1(a)). This panel displays the overall relative ion temperature perturbation with height.

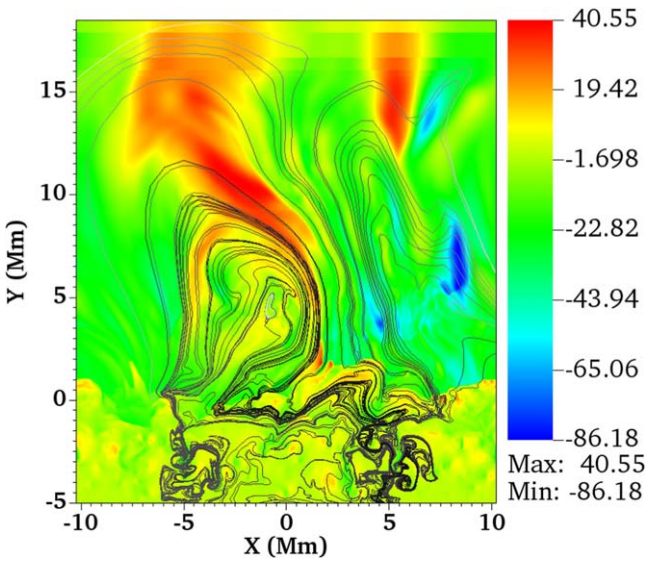

Figure 5. Snapshot of the spatial profile of the vertical component of the ion velocity, V_{iy}, measured in km s^{-1} at $t = 8870$ s. This profile provides an insightful visualization of ion motion, highlighting regions of ascent (red patches) and descent (blue patches) of plasma.

layers of the solar atmosphere, highlighting the presence of outflows. This flow is presumably not very different from that in single-fluid MHD simulations (V. H. Hansteen et al. 2010). From Figure 7(a), we can infer that ion-neutral drag ($V_i - V_n$) attains small values. The hot and tenuous plasma outflows are accompanied by the two-fluid waves (K. Murawski et al. 2022). The contour plot of the wave period calculated using the Fourier spectrum of V_{iy} (Figure 7(b)) illustrates the two-fluid waves (Section 4.3)). Due to very small resistivity in the lower corona, a large chunk of plasma can be seen frozen to the distorted and elongated magnetic field lines (Figure 5). This frozen plasma may escape into the upper layers of the solar atmosphere, forming plasma outflows and downfalls at some locations (the narrow blue patches) due to gravitational force. One may find an apparent contradiction between the closed magnetic field lines in the solar corona and the generation of the plasma outflows, which is typically associated with open magnetic field lines (K. Murawski et al. 2022). However, we can expect plasma outflows even in a closed-magnetic-field configuration. One of the possible reasons for this here is the presence of a concave magnetic field pointing upward, which moves and drags ions with it. Additionally, the plasma $\beta << 1$ in the lower corona further supports the magnetic field governing the plasma flow. From the legend bar, we can also infer that the outflows here have a high magnitude of vertical velocity ($V_{iy} \approx 40$ km s^{-1}).

The generated oscillatory movements in the plasma, as waves are excited and propagate through the upper layers of the solar atmosphere, cause periodic fluctuations in the velocity of the ions. These variations appear as quasiperiodic red and blue bands, as illustrated in the corresponding time–distance plot for V_{iy} collected along the y-direction at $x = 0$ (Figure 6(a)). A horizontally averaged plot shows a similar but distinct quasiperiodic pattern for $\langle V_{iy} \rangle_x$ (Figure 6(c)) that is defined as

$$\langle V_{iy} \rangle_x = \frac{1}{x_2 - x_1} \int_{x_1}^{x_2} V_{iy}\, dx, \tag{22}$$

where $x_2 = -x_1 = 10.24$ Mm. Analysis of both time–distance plots reveals that these bands predominantly align parallel to the y-axis, indicating the vertical propagation of waves within the solar atmosphere. We note that the red and blue bands are clearer in a later plot, because the averaging process smoothens out the horizontal variations of the ion velocity.

Plasma outflows may be a potential candidate for the solar wind origin; see, e.g., D. Wójcik et al. (2019a). Figures 6(b) and (d) illustrate, respectively, the time-averaged profiles for V_{iy} (denoted by $\langle V_{iy} \rangle_t$ and $\langle V_{iy} \rangle_{x,t}$) defined in a manner similar to Equation (21). Overall, we note that both panels show similar features, where positive values correspond to upflows

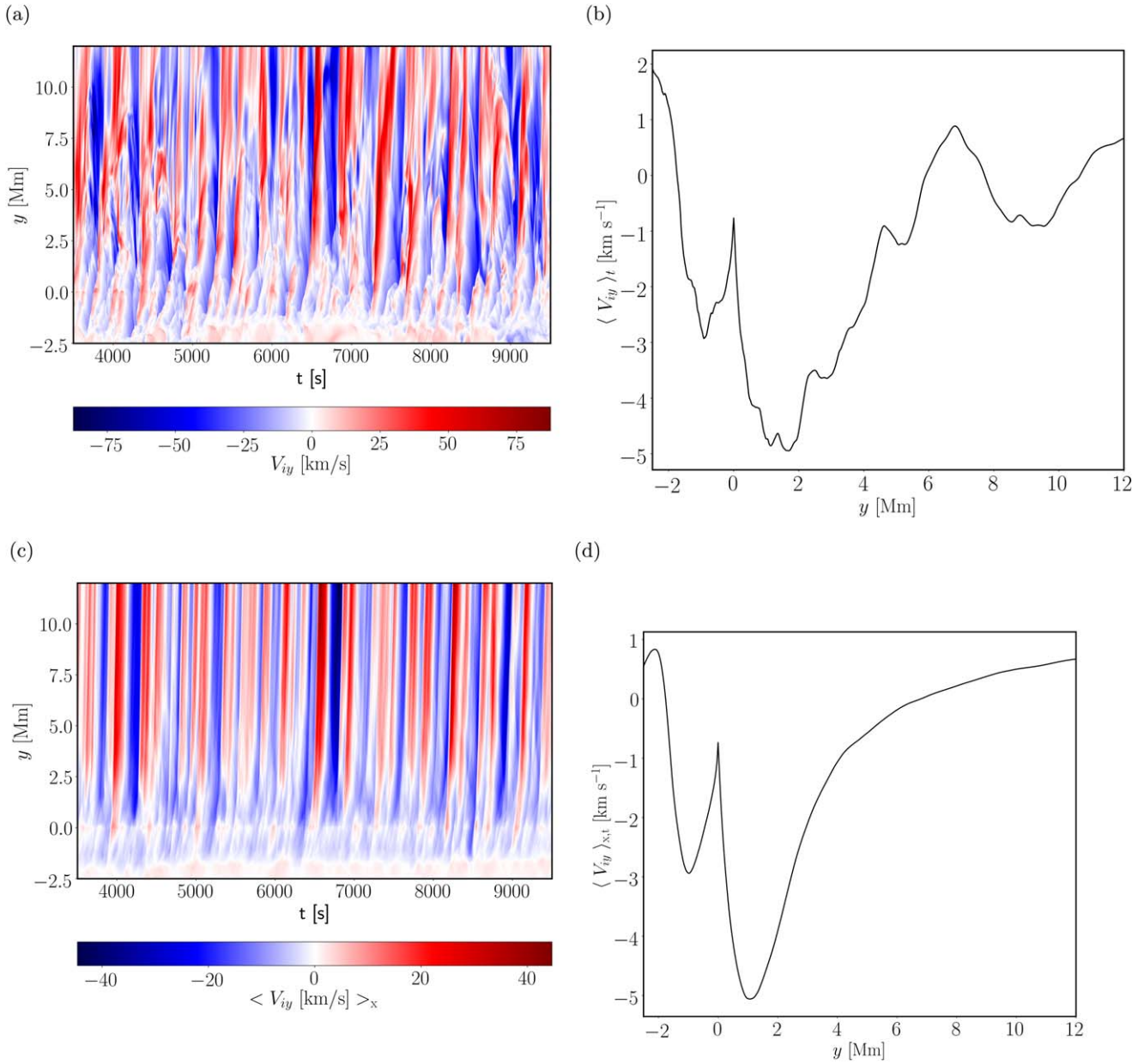

Figure 6. (a) and (c) Time–distance plots for the vertical component of the ion velocity (V_{iy}), measured in km s^{-1}. (b) and (d) The corresponding time-averaged profile of V_{iy} vs. height (y). The top panels correspond to the slit taken at $x = 0$ Mm along the y-direction, while the bottom panels correspond to the horizontal average. These profiles represent the variation in the velocity of ions in space and time. All the panels are akin to the spatial profile shown in Figure 5.

and negative values to downflows. It is also clear that up to a certain height, more downfalls are visible than upflows. This behavior is expected, due to the presence of the magnetic arcade instead of straight magnetic field lines threaded in a solar atmosphere; for example, see Figure 1 in K. Murawski et al. (2022). The arcade can trap plasma to some extent. However, even in this magnetic setup, plasma escapes through outflows at higher altitudes. The trajectory of $\langle V_{iy} \rangle_{x,t}$ (Figure 6(d)) shows smoother behavior with height, indicating a general trend of increasing with height above the transition region. Such plasma outflows are very important, as they may contribute to the solar wind in the upper layer of the solar atmosphere and may ultimately alter the quantities of the solar wind. A detailed review of plasma outflows has recently been conducted by H. Tian et al. (2021).

4.3. Ion-neutral Drift in the Solar Atmosphere and Wave Periods

The collisional coupling between ions and neutrals in the higher layers of the solar atmosphere is weak, leading to nonzero ion-neutral drift. This ion-neutral velocity drift damps the generated waves due to energy and momentum transfer (G. Haerendel 1992). The time–distance plot of the vertical component of the ion-neutral drift is illustrated in Figure 7(a), highlighting the distinct regions of interest, particularly above the photosphere. The upper chromosphere, transition region, and lower corona see an increase in the ion-neutral drift due to the progressive decoupling with height between the neutral fluid and charged species. In such regions, we observe max $|V_{iy} - V_{ny}| \approx 0.04$ km s^{-1}. We note that even this small magnitude of velocity drift results in appreciable energy flux

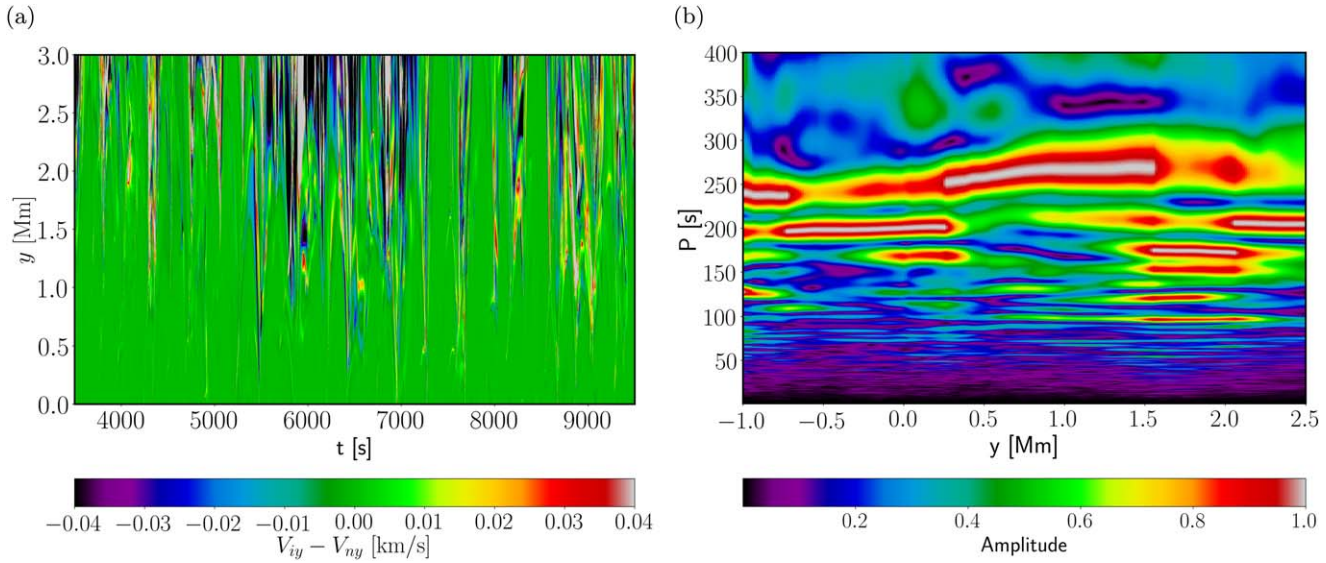

Figure 7. (a) Time–distance plot for ion and neutral vertical velocity drift, expressed in kilometers per second, gathered along the y-axis at $x = 0$. This figure highlights regions of increased velocity drift. (b) Wave periods (P) as a function of height (y). In this plot, the wave period is computed using the Fourier transform of the ion-vertical velocity $V_{\rm iy}$, as illustrated in Figure 5, and the minimum/maximum Fourier power amplitude is normalized to 0/1.

(see Equations (11) and (12) as well as Figure 3). In contrast, the ions and the neutrals are strongly coupled within and below the photosphere ($y \leqslant 0.5$ Mm). Notably, the amplitude of the ion-neutral drift observed in our current model is much smaller compared to the result presented by K. Murawski et al. (2022; see their Figure 3). This discrepancy may be attributed to the noninvolvement of a self-consistent ionization and recombination process. Consequently, certain collisional interactions in the present model may be less frequent, resulting in reduced velocity drift between ions and neutrals. We deduce that ion-neutral drift plays an essential role when fully formed granulation-stimulated flows of larger amplitude propagate in the solar atmosphere.

The stratified solar atmosphere influences wave propagation and their corresponding wave periods (H. Lamb 1917; L. Biermann 1946; M. Schwarzschild 1948). Granulation excites a broad spectrum of waves (V. Nakariakov 2020; S. Dey et al. 2022), including magnetoacoustic-gravity waves, neutral acoustic-gravity waves, and Alfvén waves (D. Wójcik et al. 2019b; B. Kuźma et al. 2021a; R. J. Morton et al. 2023), which propagate into the upper atmospheric layers. We must appreciate that the spectra of such excited waves remain indistinguishable, and it is difficult to visualize each separately. Examining the temporal plasma characteristics using Fourier power analysis reveals a spectrum with various periods. Figure 7(b) displays such an analysis of wave periods (P) versus height (y), derived from the Fourier transformation (contour plot) corresponding to the signal ion-vertical velocity $V_{\rm iy}$ (Figure 5). The obtained plot provides a visual representation of the propagating wave periods in distinct layers of the solar atmosphere. The dominant wave period of 250 s propagating in the top convection zone, photosphere, and lower chromosphere decreases to 150–200 s values in the upper chromosphere and lower corona. This reduction in wave period occurs in the region where the ion-neutral drift increases (see Figure 7(a)) and may result from the cutoff period $P_{\rm cut\text{-}off}$. Mainly, waves are propagating for $P < P_{\rm cut\text{-}off}$ but become evanescent in the other extreme. For a recent discussion, see B. Kuzma et al. (2024), who reported similar findings of wave period reduction in their numerical simulations of granulation-excited two-fluid waves.

5. Summary and Conclusions

Our results can be summarized as follows. In the present study, we have performed 2.5D numerical experiments for a partially ionized solar atmosphere to investigate the propagation and dissipation of granulation-generated waves. Our model considers nonadiabatic and nonideal effects, without considering the self-consistent ionization and recombination. We have studied, in general, these waves for insights into contributions to the heating of the chromosphere and plasma outflows. The model illustrates that self-generated and self-evolving convection beneath the photosphere, combined with the presence of a single isolated magnetic arcade—a curved structure of magnetic field lines connecting two regions of opposite polarity in the quiet region of the solar surface—facilitates the generation of a broad spectrum of waves in two-fluid plasma. From the obtained numerical results, we conclude that a part of the energy carried by the excited waves dissipates due to ion-neutral collisions, leading to localized heating of the upper photosphere and chromosphere. Moreover, such waves also give rise to plasma outflows, which, higher up, may contribute to the solar wind.

While the present paper addresses some specific aspects of the localized heating problem and plasma outflows, a study offering a more qualitative and quantitative picture has yet to be performed. Recently, D. Przybylski et al. (2022) reported the importance of nonequilibrium (NE) and non–local thermodynamic equilibrium (NLTE) impacts on chromospheric structure and dynamics. Our understanding of chromosphere heating and dynamics may be improved by including NE and NLTE methods. A. J. Finley et al. (2022) highlighted the function of small-scale vortex motions in heating and accelerating coronal plasma, demonstrating how photospheric flows twist the coronal magnetic field and cause torsional Alfvén waves (see also J. Liu et al. 2019). Additionally, S. Shelyag et al. (2011) showed how small-scale magnetic and nonmagnetic vortices are generated in the solar photosphere. This may support our results by highlighting the importance of small-scale dynamics and wave propagation in the solar atmosphere. It

is, however, worth mentioning that trying to fit all the necessary physics into one single atmospheric model would be a highly challenging task. In other words, the primary physical processes behind driving this thermalized energy in the atmospheric layers are currently unclear and active areas of research. A more sophisticated and comprehensive study of tracing the energy transfer from the cooler lower layers to the hotter outer solar atmospheric layers has yet to be achieved, to provide an accurate and more quantitative description of the solar atmosphere.

Acknowledgments

This work was carried out as part of the Space Weather Awareness Training (SWATNet) project, funded by the European Union's Horizon 2020 research and innovation program under grant agreement No. 955620. M.K. gratefully acknowledges the support received from the Polish National Agency of Academic Exchange (NAWA) under the framework of the University of M. Curie-Skłodowska (UMCS) Doctoral Schools—Your Success in a Globalized World of Science to support the present work further. The work of K.M. was done within the framework of the project from the Polish Science Center (NCN) with grant No. 2020/37/B/ST9/00184. S.P. acknowledges support from the projects C14/19/089 (C1 project Internal Funds KU Leuven), G0B5823N and G002523N (WEAVE; FWO-Vlaanderen), 4000134474 (SIDC Data Exploitation, ESA Prodex-12), and Belspo project B2/191/P1/SWiM. R.E. thanks NKFIH OTKA (Hungary, grant No. K142987) for its support. This work was also supported by the NKFIH Excellence Grant TKP2021-NKTA-64. R.E. is grateful to the STFC (UK, grant No. ST/M000826/1) and PIFI (China, grant No. 2024PVA0043). Dr. Dariusz Wójcik developed the JOANNA code, with further contributions from Dr. Luis Kadowaki and Mr. Piotr Wołoszkiewicz. M.K. acknowledges Dr. Luis Kadowaki's suggestions for shaping the draft at its initial development. We also kindly acknowledge the unknown referee, whose comments and suggestions greatly helped to shape the paper. Numerical simulations were run on the LUNAR cluster at the Institute of Mathematics at M. Curie-Skłodowska University in Lublin, Poland. We gratefully acknowledge Poland's high-performance computing infrastructure, PLGrid (HPC Centers: ACK Cyfronet AGH), for providing computer facilities and support within computational grant No. PLG/2022/015868. We visualized the simulation data using the ViSIt software package (H. Childs et al. 2012) and Python scripts.

ORCID iDs

S. Poedts https://orcid.org/0000-0002-1743-0651

References

Abbett, W. P., & Fisher, G. H. 2012, SoPh, 277, 3
Alfvén, H. 1942, Natur, 150, 405
Avrett, E. H., & Loeser, R. 2008, ApJS, 175, 229
Ballester, J. L., Alexeev, I., Collados, M., et al. 2018, SSRv, 214, 58
Biermann, L. 1946, NW, 33, 118
Bogdan, T. J., Hansteen, M. C., McMurry, A., et al. 2003, ApJ, 599, 626
Braginskii, S. I. 1965, RvPP, 1, 205
Carlsson, M., & Stein, R. F. 1994, ApJL, 440, L29
Childs, H., Brugger, E., Whitlock, B., et al. 2012, VisIt: An End-User Tool For Visualizing and Analyzing Very Large Data (Chapman and Hall/CRC), 357
Courant, R., Friedrichs, K., & Lewy, H. 1928, MatAn, 100, 32
Dedner, A., Kemm, F., Kröner, D., et al. 2002, JCoPh, 175, 645
Dey, S., Chatterjee, P., M, O. V. S. N., et al. 2022, NatPh, 18, 595
Durran, D. R. 2010, Numerical Methods for Fluid Dynamics: With Applications to Geophysics, Vol. 32 (Springer Science & Business Media)
Erdélyi, R., & James, S. P. 2004, A&A, 427, 1055
Finley, A. J., Brun, A. S., Carlsson, M., et al. 2022, A&A, 665, A118
Haerendel, G. 1992, Natur, 360, 241
Hansteen, V. H., Hara, H., De Pontieu, B., & Carlsson, M. 2010, ApJ, 718, 1070
James, S., & Erdélyi, R. 2002, in Solar Variability: From Core to Outer Frontiers, Vol. 506 (European Space Agency, 2002), 649
James, S., Erdélyi, R., & De Pontieu, B. 2003, A&A, 406, 715
Jess, D. B., Mathioudakis, M., Erdélyi, R., et al. 2009, Sci, 323, 1582
Judge, P. G. 2020, MNRAS, 498, 2018
Judge, P. G., Tarbell, T. D., & Wilhelm, K. 2001, ApJ, 554, 424
Khodachenko, M., Arber, T., Rucker, H. O., & Hanslmeier, A. 2004, A&A, 422, 1073
Khomenko, E., Collados, M., Díaz, A., & Vitas, N. 2014, PhPl, 21, 092901
Kumar, M., Murawski, K., Kadowaki, L., Kuzma, B., & Kilpua, E. 2023, A&A, 681, A60
Kuzma, B., Kadowaki, L. H. S., Murawski, K., et al. 2024, RSPTA, 382, 20230218
Kuźma, B., Murawski, K., Kayshap, P., et al. 2017, ApJ, 849, 78
Kuźma, B., Murawski, K., Musielak, Z. E., Poedts, S., & Wójcik, D. 2021a, A&A, 652, A88
Kuźma, B., Murawski, K., Musielak, Z. E., Poedts, S., & Wójcik, D. 2021b, A&A, 652, A88
Kuźma, B., Wójcik, D., & Murawski, K. 2019, ApJ, 878, 81
Lamb, H. 1917, RSPSA, 93, 114
Leake, J. E., Arber, T., & Khodachenko, M. 2005, A&A, 442, 1091
Leake, J. E., DeVore, C. R., Thayer, J. P., et al. 2014, SSRv, 184, 107
Leake, J. E., Lukin, V. S., Linton, M. G., & Meier, E. T. 2012, ApJ, 760, 109
Lites, B., Rutten, R., & Kalkofen, W. 1993, ApJ, 414, 345
Liu, J., Nelson, C. J., Snow, B., Wang, Y., & Erdélyi, R. 2019, NatCo, 10, 3504
Low, B. 1985, ApJ, 293, 31
Maneva, Y. G., Laguna, A. A., Lani, A., & Poedts, S. 2017, ApJ, 836, 197
Martínez-Sykora, J., Szydlarski, M., Hansteen, V. H., & De Pontieu, B. 2020, ApJ, 900, 101
Mignone, A., Ugliano, M., & Bodo, G. 2009, MNRAS, 393, 1141
Miyoshi, T., & Kusano, K. 2007, AGU Fall Meeting Abstracts, 2007, SM41A–0311
Moore, R., & Fung, P. 1972, SoPh, 23, 78
Morton, R. J., Sharma, R., Tajfirouze, E., & Miriyala, H. 2023, RvMPP, 7, 17
Murawski, K., Musielak, Z., Poedts, S., Srivastava, A., & Kadowaki, L. 2022, Ap&SS, 367, 111
Murawski, K., Srivastava, A. K., McLaughlin, J. A., & Oliver, R. 2013, SoPh, 283, 383
Nakariakov, V. 2020, in Oxford Research Encyclopedia of Physics
Niedziela, R., Murawski, K., & Poedts, S. 2021, A&A, 652, A124
Osterbrock, D. E. 1961, ApJ, 134, 347
Pelekhata, M., Murawski, K., & Poedts, S. 2021, A&A, 652, A114
Piddington, J. H. 1956, MNRAS, 116, 314
Priest, E. 2014, Magnetohydrodynamics of the Sun (Cambridge: Cambridge Univ. Press)
Przybylski, D., Cameron, R., Solanki, S., et al. 2022, A&A, 664, A91
Schwarzschild, M. 1948, ApJ, 107, 1
Shelyag, S., Keys, P., Mathioudakis, M., & Keenan, F. P. 2011, A&A, 526, A5
Shelyag, S., Mathioudakis, M., & Keenan, F. P. 2012, ApJL, 753, L22
Skirvin, S., Verth, G., González-Avilés, J. J., et al. 2023, AdSpR, 71, 1866
Soler, R., Ballester, J., & Zaqarashvili, T. 2014, A&A, 573, A79
Soler, R., Ballester, J., & Zaqarashvili, T. 2015, A&A, 573, A79
Spitzer, L. 1962, AmSci, 50, 473
Stein, R., & Nordlund, Å. 1998, ApJ, 499, 914
Stein, R. F., & Leibacher, J. 1974, ARA&A, 12, 407
Tian, H., Harra, L., Baker, D., Brooks, D. H., & Xia, L. 2021, SoPh, 296, 1
Vranjes, J., & Krstic, P. S. 2013, A&A, 554, A22
Wang, Y., Yokoyama, T., & Iijima, H. 2021, ApJL, 916, L10
Wójcik, D., Kuźma, B., Murawski, K., & Musielak, Z. 2020, A&A, 635, A28
Wójcik, D., Kuźma, B., Murawski, K., & Srivastava, A. 2019a, ApJ, 884, 127
Wójcik, D., Murawski, K., & Musielak, Z. 2019b, ApJ, 882, 32
Wójcik, D., Murawski, K., & Musielak, Z. E. 2018, MNRAS, 481, 262
Yadav, N., Cameron, R. H., & Solanki, S. K. 2021, A&A, 652, A43
Yang, S., & Xiang, Y. 2016, ApJL, 819, L24
Yang, Z., Bethge, C., Tian, H., et al. 2020, Sci, 369, 694
Zaqarashvili, T. V., Khodachenko, M. L., & Rucker, H. O. 2011, A&A, 529, A82